



Photocatalytic performance of Sn-doped TiO₂/reduced graphene oxide composite materials



Thuy-Duong Nguyen-Phan ^a, Viet Hung Pham ^a, Jin Suk Chung ^a, Manish Chhowalla ^b, Tewodros Asefa ^{c,d}, Woo-Jae Kim ^e, Eun Woo Shin ^{a,*}

^a School of Chemical Engineering and Bioengineering, University of Ulsan, Daehakro 93, Nam-gu, Ulsan 680-749, South Korea

^b Department of Materials Science and Engineering, Rutgers, The State University of New Jersey, 610 Taylor Road, Piscataway, NJ 08854, USA

^c Department of Chemistry and Chemical Biology, Rutgers, The State University of New Jersey, 610 Taylor Road, Piscataway, NJ 08854, USA

^d Department of Chemical and Biochemical Engineering, Rutgers, The State University of New Jersey, 98 Brett Road, Piscataway, NJ 08854, USA

^e Department of Chemical and Environmental Engineering, Gachon University, San 65, Bokjeong-dong, Sujeong-gu, Sungnam, Gyeonggi-do 461-701, South Korea

ARTICLE INFO

Article history:

Received 22 May 2013

Received in revised form

17 December 2013

Accepted 23 December 2013

Available online 3 January 2014

Keywords:

TiO₂

Sn doping

Graphene

Nanocomposite

Photocatalysis

ABSTRACT

Composite materials of Sn-doped TiO₂ nanoparticles (4–6 nm) uniformly anchored onto reduced graphene oxide (RGO) sheets were fabricated by a hydrothermal process. When compared with an undoped TiO₂/RGO composite material, the partial substitution of Sn⁴⁺ for Ti⁴⁺ in TiO₂/RGO in different doping concentrations not only increased the specific surface area, but also narrowed the band gap energy of the material. It also resulted in a shift in the photoresponse of the material into the visible light region, an increase in the relative intensity of its Raman (D/G) band, and changes in its X-ray photo-electron spectra; these results implied strong interactions between the Sn species and nanosized TiO₂ as well as between the TiO₂ and RGO layers. The presence of RGO led to enhanced adsorptivity of methyl orange onto the material compared with that of either pure TiO₂ or Sn-doped TiO₂. Increasing the Sn dopant content to optimal value facilitated photoactivity under both UV and visible light irradiation. The incorporation of both RGO and Sn dopants significantly modified the electronic structure of TiO₂, altering the electron transfer direction and efficiently prohibiting the recombination of photo-induced charge carriers.

© 2013 Elsevier B.V. All rights reserved.

1. Introduction

Graphene, a single-atom-thick planar sheet of sp²-bonded carbon atoms, has become one of the most attractive materials due to its fascinating chemical and physical properties as well as its diverse potential applications [1–7]. One of the most exciting approaches successfully applied to exploit the unique structures and properties of graphene for various applications has been by combining graphene (GP) or reduced graphene oxide (RGO) with other inorganic and/or organic constituents [2,8–19]. This allows the properties of each constituent to be preserved or significantly altered, affording interesting and unprecedented new properties, thus broadening the potential applications of the materials. Composite materials composed of metal oxides have been extensively studied for various applications, especially in the field of photocatalysis for environmental remediation applications [14,17]. While TiO₂ and SnO₂ have been considered

two of the most popular and useful semiconductor photocatalysts, the hybrid systems they form in combination with GP or RGO sheets have attracted more attention because they have improved photocatalytic activities and other useful properties for photocatalysis [17,20–25]. For example, GP/RGO nanosheets can render significantly increased porosity and improved electron transport pathways for the metal oxides, making the latter exhibit better photocatalytic activities. The structure of composite materials containing metal oxides and GP/RGO nanosheets can also significantly enhance the accessibility, diffusion, and adsorption of organic molecules while facilitating the separation of UV-photogenerated electron–hole pairs, resulting in higher photocatalytic conversion [15,20,21,24,26]. Furthermore, owing to the roles of GP and RGO as photosensitizers [20,21,26,27], composite materials containing GP or RGO can function better with visible light during photocatalysis, a need that is often not met by many conventional laboratory-scale photocatalysts in practical applications.

Similarly, metallic or non-metallic elements can also be used for doping metal oxides and improve the energy levels of the metal oxides [28,29]. This has, in fact, been among the well-known strategies used to inhibit the recombination of excited charge carriers

* Corresponding author. Tel.: +82 52 259 2253; fax: +82 52 259 1689.

E-mail addresses: ewshin@mail.ulsan.ac.kr, ewshin@ulsan.ac.kr (E.W. Shin).

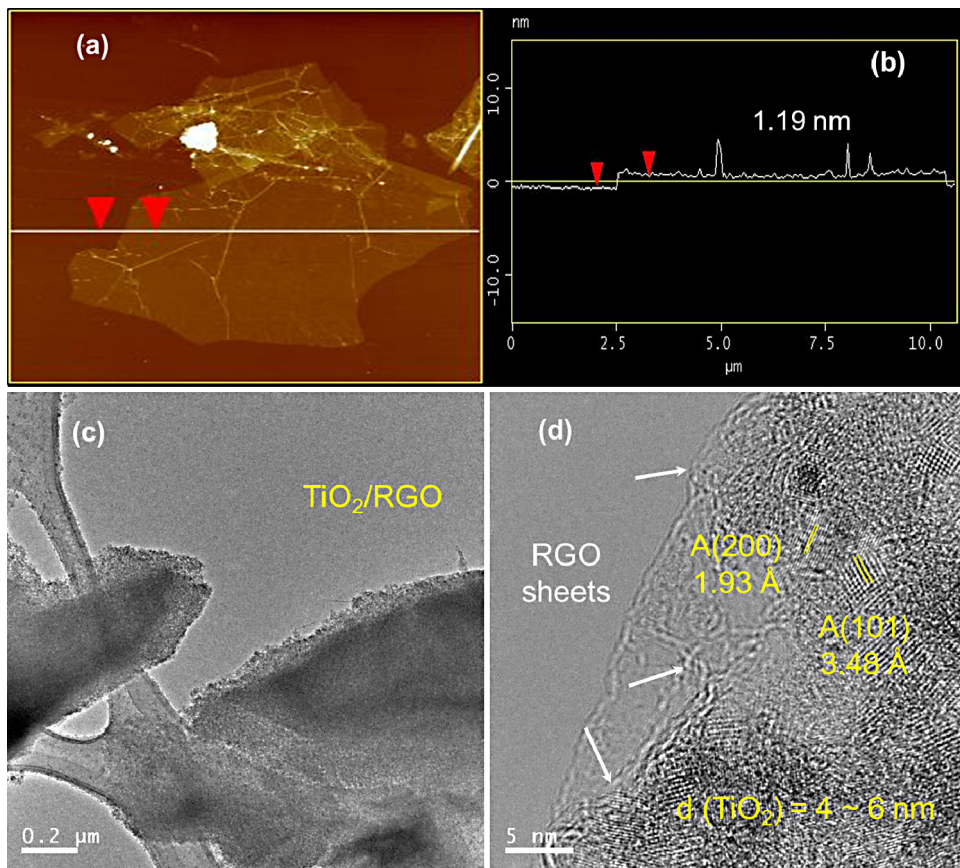


Fig. 1. (a) AFM image and (b) height profile of the GO precursor; (c and d) HR-TEM images of the TiO₂/RGO composite (denoted as STG-0).

in semiconducting metal oxides, extend their photoresponse to the visible light range, and thereby increase their photocatalytic efficiency. Among many metal-doped metal oxide materials, Sn⁴⁺-doped TiO₂ is a notable example, which can be synthesized by numerous methods, including sol-gel, hydrothermal, and coprecipitation processes [30–35]. The resulting doped material has been shown to have significantly improved photocatalytic activity toward the degradation organic pollutants under UV and visible light irradiation [30,31,33].

Although the effect of combining SnO₂ with TiO₂; TiO₂ with GP/RGO; and SnO₂ with GP/RGO for enhancing the photocatalytic activity of the materials for degradation of organic compounds (or for improving the photophysical properties of the materials in dye-sensitized solar cells) has been extensively explored, the effect of integrating both TiO₂ and SnO₂ with GP or RGO layers has not been reported yet. Very few reports have recently concerned about such integrated systems composed of two or more active components (*via* metal deposition, doping or mixed oxides) with GP or RGO that greatly manifests new, fascinating and tunable properties, *i.e.* Fe-TiO₂/GP, Pt-TiO₂/GP, Ag-TiO₂/RGO, LiFePO₄/C/GP, GP/Fe₃O₄@carbon, α-Fe₂O₃/GP/BiV_{1-x}Mo_xO₄, TiO₂@Co₃O₄/GP, Ni(OH)₂/CoO/RGO, GP-ZnO-Au [36–42]. Exploring such new composite materials possessing high surface area, a good dispersion of small semiconductor particles on a large 2D carbonaceous sheet, and improved electronic/optical properties is interesting because such materials are expected to have higher photocatalytic activity under both UV and visible light irradiations.

Therefore, herein we investigated for the first time the photocatalytic activity of a series of composite materials containing Sn-doped TiO₂ nanoparticles anchored onto the surface of RGO sheets. The resulting materials were found to have high photocatalytic activity for wastewater remediation. The composite

materials were fabricated by a hydrothermal process, and their physico-chemical and optical properties were determined by several techniques. The higher photocatalytic activity of the materials was attributed to the synergistic effect between RGO and Sn dopants, which was evaluated through their photocatalytic activity toward the photodegradation of methyl orange (MO) under UV and visible light illumination.

2. Experimental

2.1. Synthesis of STG composite materials

Tin (IV) chloride fuming (Riedel-de Haen, SnCl₄) and titanium *n*-butoxide (Aldrich, Ti(-OC₄H₉)₄) were used as TiO₂ and SnO₂ precursors. All the chemicals reagents were used as purchased without further purification.

In a typical procedure, a solution of SnCl₄ and anhydrous ethanol (40 mL) was stirred at room temperature, followed by the drop-wise addition of deionized water and HCl (37 wt%). A mixture of Ti(-OC₄H₉)₄ and acetylacetone (molar ratio of 1:2) was stirred for 90 min, then for 2 h at 313 K. Graphene oxide (GO) was synthesized from expanded graphite (grade 1721, Asbury Carbon) by a modified Hummers method [43] as described in the Supplementary material. The GO dispersion (~1 wt%) was added to the precursor solution under vigorous stirring at 313 K and then continuously stirred for 4 h. The entire solution was hydrothermally treated at 353 K for 12 h. The solid products were recovered by washing with warm ethanol and then drying overnight at 353 K. The obtained Sn-doped TiO₂/RGO composites were denoted as STG-*i*, where '*i*' is 0, 1, 2, 5, and 10 mol% Sn. Pristine TiO₂ and Sn-doped TiO₂ were

also prepared by using the same procedure, except addition of Sn and/or GO sources.

2.2. Characterization

The structure of the composite materials was probed by field-emission scanning electron microscopy (FE-SEM, JSM-600F, JEOL, Japan) and high-resolution transmission electron microscopy (HR-TEM, JEM-2100F, JEOL, Japan) using samples casted on carbon-coated Cu or Au grids. By using energy dispersive X-ray (EDX) accessory on the TEM microscope, the composition of the samples was also analyzed. Atomic force microscope (AFM) image was acquired by using a Veeco Dimension 3100 SPM (US) containing a silicon cantilever and operating in a tapping mode. X-ray diffraction (XRD) patterns were recorded on a Rigaku D/MAXZ 2500 V/PC high-power diffractometer (Japan) with Cu K α radiation ($\lambda = 1.5418 \text{ \AA}$) at a scan rate of $2^\circ(2\theta) \text{ min}^{-1}$. Raman spectra were collected using a DXR Raman microscope (ThermoFisher Scientific, USA) with 633 nm laser excitation. UV-visible diffuse reflectance spectra (UV-Vis-DRS) were obtained with a SPECORD 210 Plus spectrometer (Analytikjena, Germany). The porosity and surface area of the materials were determined with a Micromeritics ASAP 2020 instrument (USA) at -196°C . X-ray photoelectron spectra (XPS) were acquired with a K-alpha X-ray photoelectron spectrometer (XPS) (Thermo Fisher, UK).

2.3. Photocatalytic degradation evaluation

The photocatalytic activity of the STG composite materials was evaluated by analyzing the photodegradation of an aqueous solution of MO by using the materials as photocatalyst. The photocatalyst (30 mg) was first immersed in 100 mL of a solution containing MO ($C_0 = 2.5 \times 10^{-5} \text{ M}$) under constant stirring inside a chamber with a cooling fan. After adsorption of MO under dark for 2 h and reaching equilibrium, four surrounding 20 W black lights (Alim Industry Co., Korea, $\lambda_{\text{max}} = 365 \text{ nm}$) or 20 W daylight lamps (Osram, Korea, $\lambda_{\text{max}} = 545 \text{ nm}$) were switched on to irradiate the photoreactor (or the samples). The concentrations of MO were determined with a UV-Vis absorbance microplate spectrophotometer (Spectra Max® Plus 384) at $\lambda_{\text{max}} = 464 \text{ nm}$.

3. Results and discussion

3.1. Structural and physico-chemical properties of STG hybrids

First, the GO, which was used as a precursor to make the composite materials, was characterized by AFM, as shown in Fig. 1(a). The topography image shows that the GO has a smooth and large sheet-like structure with numerous wrinkles. From the height profile in Fig. 1(b), the thickness of the GO monolayer was found to be 1.19 nm.

Next, the structure of the TiO₂/RGO and Sn-TiO₂/RGO hybrid materials was examined by electron microscopy. Fig. 1(c) shows a uniform dispersion of TiO₂ nanoparticles with diameters of 4–6 nm on the RGO layers. From the high-resolution TEM image of STG-0 in Fig. 1(d), well-resolved lattice spacings of 3.48 and 1.93 Å were observed, which corresponded to the *d*-spacing of the (1 0 1) and (2 0 0) plane for anatase TiO₂, respectively. Similarly, the TEM micrographs of the STG-2 composite materials (Fig. 2) revealed that the large surface of the RGO layers was well-decorated with nano-sized Sn-doped TiO₂ particles. The HR-TEM/EDX spectrum (inset of Fig. 2(b)) showed that STG-2 contained C, O, Ti, and Sn. The image of lattice fringes in Fig. 2(c) obviously shows that the average size of the GO-anchored Sn-doped TiO₂ nanoparticles was quite smaller than pure TiO₂, with interplanar spacing *d* = 3.55–3.57 Å and *d* = 2.36–2.38 Å corresponding to crystal plane (1 0 1) and (0 0 4)

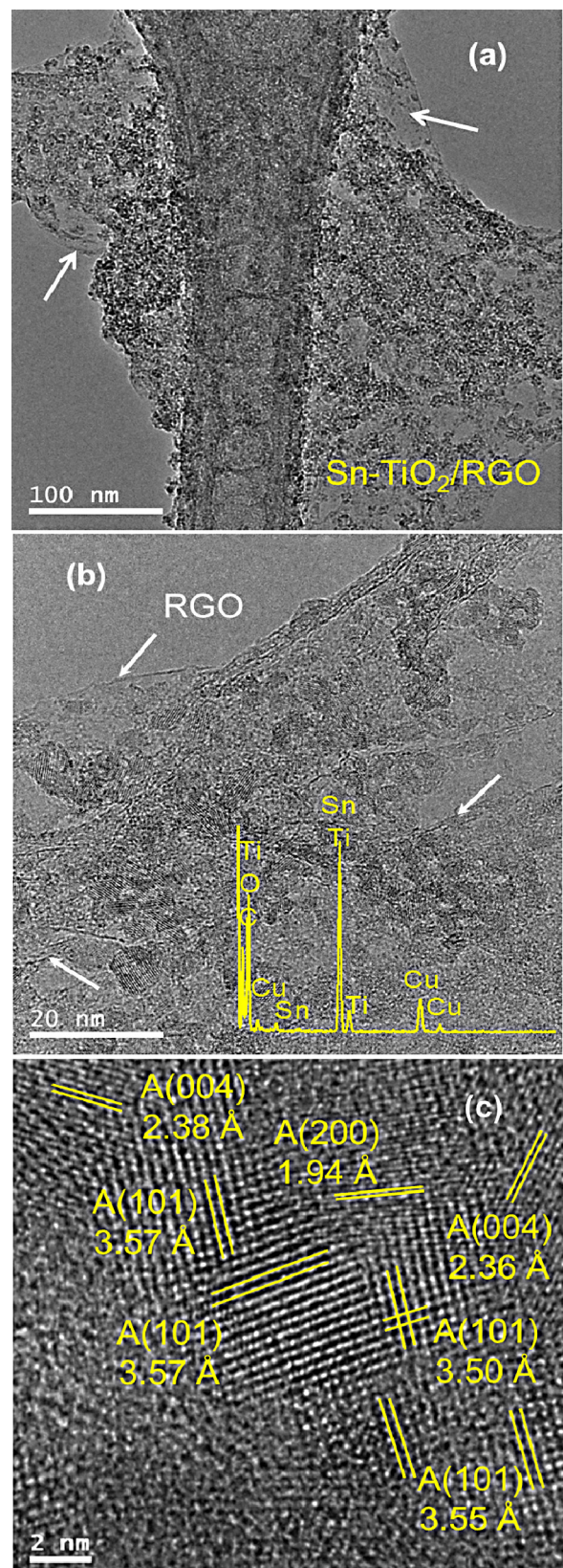


Fig. 2. Typical HR-TEM micrographs of the STG-2 composite (the TEM/EDX spectrum used for elemental analysis is shown in the inset of (b)).

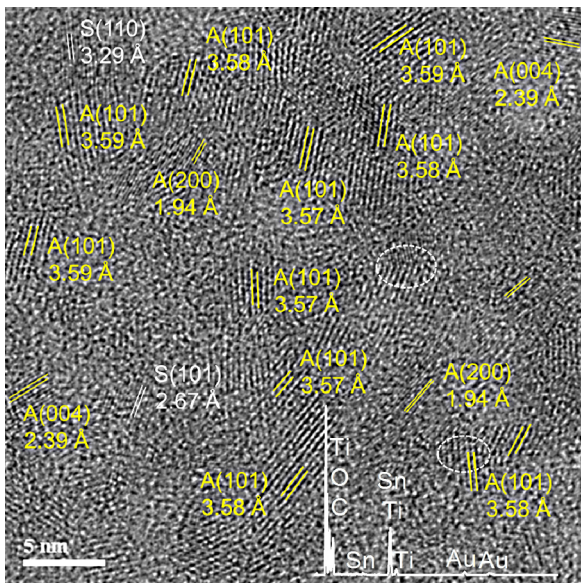


Fig. 3. HR-TEM image and EDX spectrum of Sn-doped TiO_2 /RGO composite containing 10 mol% Sn doping.

of anatase, which are larger than those of pristine TiO_2 , indicating the lattice expansion when Sn dopants with larger ionic radius ($\text{Sn}^{4+} = 0.69 \text{ \AA}$, $\text{Ti}^{4+} = 0.605 \text{ \AA}$) [44] are introduced. The distribution of Ti, O, C and Sn elements in STG-2 composite can be seen on the elemental mapping from both FE-SEM and HR-TEM, where the relative location of each constituent can be spotted in different colors, shown in Figs. S1 and S2 in Supplementary materials. Anatase nanoparticles were uniquely found onto RGO sheets with different crystal planes, such as $d_{101} = 3.52\text{--}3.60 \text{ \AA}$, $d_{004} = 2.41 \text{ \AA}$. The distortion or dislocation was also determined due to the electric stress [45,46] originating from ionic radii mismatch via doping. Thus, such lattice increment and crystal defects in present study clearly confirm the substitution of Sn species into the TiO_2 framework decorating the RGO sheets.

In addition, HR-TEM image of STG-10 composite is shown in Fig. 3 accompanied with EDX spectrum. It can be seen that small nanoparticles were anchored onto carbonaceous sheet, possessing dominant doped anatase TiO_2 structure with distinct crystal planes, i.e. $d_{101} = 3.57\text{--}3.59 \text{ \AA}$, $d_{004} = 2.39 \text{ \AA}$, $d_{200} = 1.94 \text{ \AA}$, much larger than those of pristine TiO_2 . The lattice increment obviously indicates that Sn species are well incorporated into TiO_2 lattice. Furthermore, small portion of free SnO_2 particle was observed with lattice spacings of 3.29 and 2.67 \AA which are representative of (110) and (101) planes, respectively. This result significantly indicates excess Sn doping concentration induces the additional crystallographic phase of dopant in form of small dispersed clusters apart from Sn-doped TiO_2 particles onto RGO sheets. The composition and elemental distribution of Ti, O, Sn, and C were also demonstrated by HR-TEM/EDX and mapping shown in Fig. S3 in Supplementary materials.

XRD patterns of the nanosized TiO_2 and STG-*i* hybrids are shown in Fig. 4. A series of (101), (004), (200), (105), (211), (204), and (215) reflections at $2\theta = 25.4^\circ$, 37.9° , 48.1° , 54.2° , 55.1° , 62.6° , and 75.1° , respectively, were observed in the TiO_2 sample, which is in good agreement with the reference spectrum for the anatase structure (JCPDS 21-1272, I4₁/amd). Although the GO precursor showed a representative (002) reflection at $2\theta = 10.5^\circ$ with an interlayer spacing of 8.5 \AA (see Fig. S4 in Supplementary material), no peak from the RGO layers can be detected in any of the composite materials, indicating that carbonaceous sheets were well-exfoliated and covered by metal oxides. In addition, no

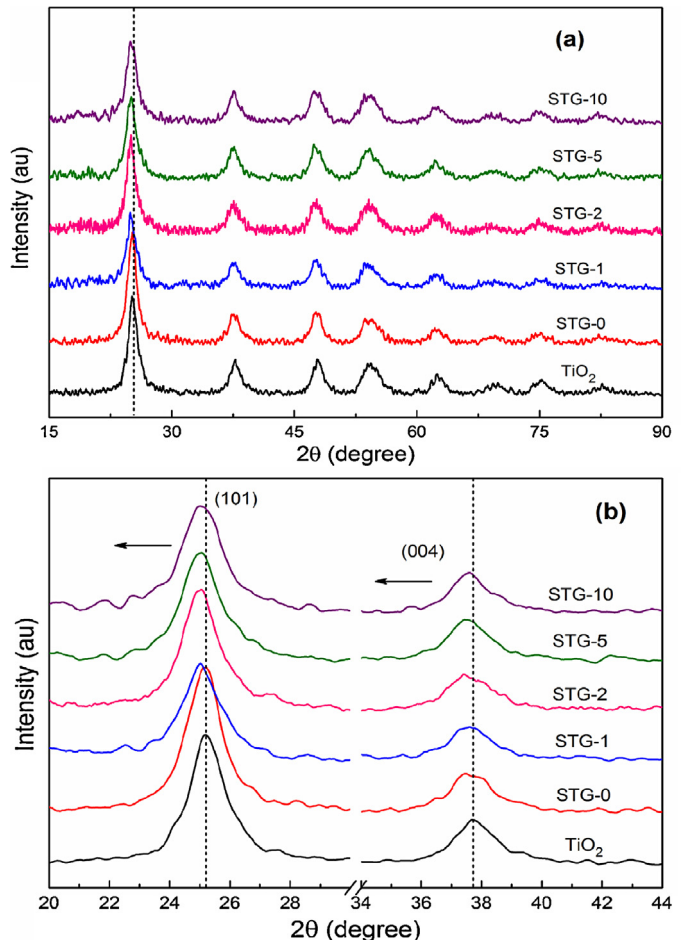


Fig. 4. (a) Full wide-angle XRD and (b) re-scaled patterns of the TiO_2 and STG-*i* samples.

diffraction from Sn or SnO_2 phases (JCPDS 41-1445, P4₂/mnm) was observed, demonstrating the complete dissolution of Sn^{4+} cations to form Sn–O–Ti bonding and/or the formation of very small SnO_2 clusters well-dispersed among anatase TiO_2 crystallites. Slight shift in (101) and (004) diffractions in STG samples toward smaller 2-theta values, the peak intensity decrease and the peak width broadening occurred when Sn was doped into the material (seen in re-scaled patterns in Fig. 4(b)), indicating an increase in the lattice parameter and the decrease in average grain size stemming from the increase in disorder with the substitution of Sn into TiO_2 lattice sites. The XRD results are consistent with the aforementioned HR-TEM findings. Due to the difference in ionic radii ($\text{Sn} = 69 \text{ pm}$, $\text{Ti} = 53 \text{ pm}$, $\text{Sn}^{4+} = 0.69 \text{ \AA}$, $\text{Ti}^{4+} = 0.605 \text{ \AA}$) [44], a lattice mismatch during the partial substitution of Sn^{4+} for Ti^{4+} in the TiO_2 lattice occurred, leading to lattice distortion and the generation of edge dislocations. Nevertheless, in spite of the observation of few SnO_2 particles in HR-TEM in STG-10 sample, the absence of Sn or SnO_2 diffractions in XRD can be attributed to its low concentration that is below the instrumental detection limitation.

The Raman spectra of the GO, TiO_2 , and STG samples were obtained in order to evaluate the interaction between RGO and the inorganic component; the results are shown in Fig. 5. Numerous distinctive bands at 150 (E_g), 199 (E_g), 410 (B_{1g}), 513 ($A_{1g} + B_{1g}$), and 635 cm^{-1} (E_g) corresponding to anatase TiO_2 were detected in all samples (Fig. 5(a)), which is in good agreement with the XRD results. Two representative D and G bands at 1341 and 1589 cm^{-1} in different relative intensities (I_D/I_G) were found in the GO precursor and STG hybrid materials. These bands correspond to the

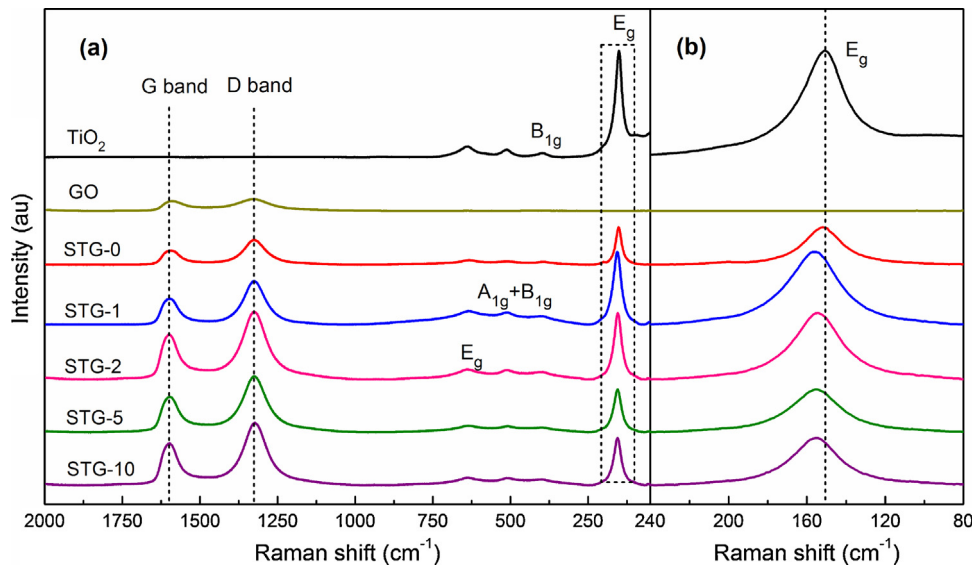


Fig. 5. (a) Full Raman spectra and (b) re-scaled spectra of GO, TiO₂, and STG-*i* composites.

breakage of symmetry by edges or a high density of defects, as well as the first-order scattering of the E_{2g} vibration mode observed for the sp² domains, respectively [47]. The I_D/I_G ratio increased from 1.12 for GO to 1.5–1.8 for the hybrids (1.78, 1.69, 1.53, 1.60, and 1.49 for 0, 1, 2, 5, and 10 mol% Sn, respectively), indicating either an increase in the average size of sp² domains or an interaction between the nanoparticles and RGO sheets. In addition, as seen in Fig. 5(b), while E_g peak of STG-0 at 150 cm⁻¹ was unchanged compared with that of pristine TiO₂, the shifts to higher wavenumber was detected in Sn-doped composites. That obviously implies the increase in surface oxygen vacancy due to doping effect and thus, the guest–host interaction [36,48].

The textural properties of the STG composites were determined via N₂ sorption measurements; the results are summarized in Table 1. The adsorption–desorption isotherms are shown in Fig. S5(a) (Supplementary material). Pure TiO₂ nanoparticles exhibited a Brunauer–Emmett–Teller (BET) surface area of 261 m² g⁻¹. The addition of RGO initially enhanced the surface area from 261 to 271 m² g⁻¹. The presence of doping Sn ions into TiO₂ led to the gradual increase in surface area up to optimal value at 2 mol% Sn, ~319 m² g⁻¹. The increase of surface area may be ascribed to the reduction in average grain size arising from the increase in disorder with the substitution of Sn ions into TiO₂. This is consistent with the HR-TEM and XRD results described above. Accordingly, as seen in Figs. 1 and 2, the RGO sheets were fully covered by abundant aggregated TiO₂ particles in STG-0 sample, whilst small particles were scattered on large exfoliated RGO surface in STG-2 composites. Herein, it can be additionally speculated the prevention of nanoparticle aggregation and restacking of RGO by doping as well as the confinement effect of RGO, efficiently separating inorganic particles one by one and thus enlarging the surface area. However, further a decrease occurred at excess amount might be due to the formation of free SnO₂ clusters highly dispersed among TiO₂ crystallites that led to the pore blocking. Such blocking was clearly elucidated by the changes in microporosity and pore size distribution. As shown in Table 1, increasing Sn content led to the decreases in both micropore areas and micropore volumes from 39.33 m² g⁻¹ and 0.0185 cm³ g⁻¹ to 25.76 m² g⁻¹ and 0.0095 cm³ g⁻¹, respectively. The mesopore sizes of STG-2, STG-5 and STG-10 were 3.04–3.12 nm, also smaller than those of other samples. Moreover, the pore size distribution in Fig. S5(b) in Supplementary materials obviously became narrower and sharper with

Sn introduction. Thus, N₂ sorption measurement demonstrates that high doping dosage has detrimental effect on the texture of the STG composite materials.

The chemical oxidation states of Ti and Sn were then elucidated based on core level XPS spectra (Fig. 6). The component peaks of the representative doublet at 458.68 and 464.40 eV in Fig. 6(a) were assigned to the Ti 2p_{3/2} and Ti 2p_{1/2} states of octahedrally coordinated Ti⁴⁺ [49]. The Sn doping induced the additional presence of lower oxidation state Ti³⁺ at 457.54 eV due to the charge imbalance upon doping. The co-existence of Ti³⁺ is well consistent with lattice increment confirmed by HR-TEM and XRD aforementioned because of larger ionic radius of Ti³⁺ (0.67 Å) [44] than that of Ti⁴⁺. It can be obviously seen that Ti 2p in STG-2 and STG-10 obviously shift toward higher binding energies, 458.76/464.56 and 458.80/464.59 eV, respectively, whereas there is unchanged in STG-1 and STG-5 composites. The peaks of Ti³⁺ state correspondingly shifted to higher binding energies. As is evident in high resolution XPS of Sn 3d in Fig. 6(b), the peak located at 486.20 eV in STG-1 composite is assigned to Sn 3d_{5/2} of Sn⁴⁺. However, we were not able to determine the broad peak at 496.45 eV as there was no precedence for this peak. The small shoulders at 485.70 and 485.80 eV were found for STG-5 and STG-10, implying the supplemental presence of Sn²⁺. The intensity of these Sn 3d peaks increased as the doping content was increased. Increasing Sn content to 2, 5 and 10 mol% led to the shift of both Sn 3d_{5/2} and Sn 3d_{3/2} to 486.80/495.65, 486.73/495.85 and 486.92/495.55 eV, respectively. Such a shift is induced by the changes in chemical state or coordinated environment due to the difference in dispersion states, ligand effect or electronic interaction between various components to form A–O–B bonding [50,32]. Thus, in this work, the shifts in both Ti 2p and Sn 3d core level spectra are attributed to a certain electron drain from Ti⁴⁺ in the oxide matrix due to the presence of Sn⁴⁺, occurring the charge transfer between two cationic species through the oxygen bridge in heterogeneous linkage of Sn–O–Ti [32,51]. The quantitative analysis revealed that the Sn/Ti ratio was 1.35% for STG-2, 2.82% for STG-5, and 3.02% for STG-10. Moreover, when compared to pristine GO, the C 1s XPS spectra in Fig. S6 (see Supplementary material) indicated the elimination of several deconvoluted peaks at higher binding energies (BE), described as oxygenate-containing functional groups, including C–OH/C(epoxy), C=O, and O–C=O groups. The existence of a C–C peak in all STG hybrids further confirmed the reduction of GO to RGO, as observed in previous reports [3–7,24,26].

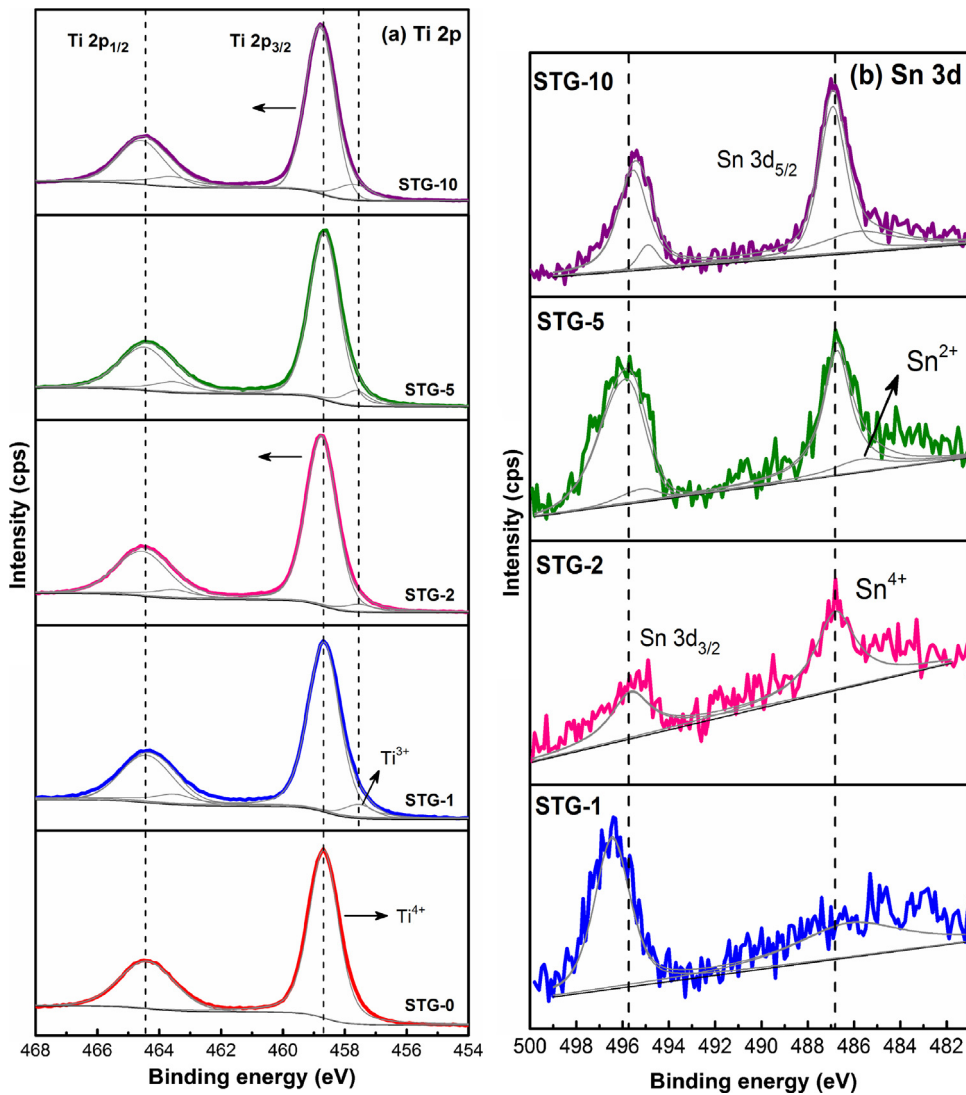


Fig. 6. XPS core-level spectra of the STG-*i* composites: (a) Ti 2p and (b) Sn 3d.

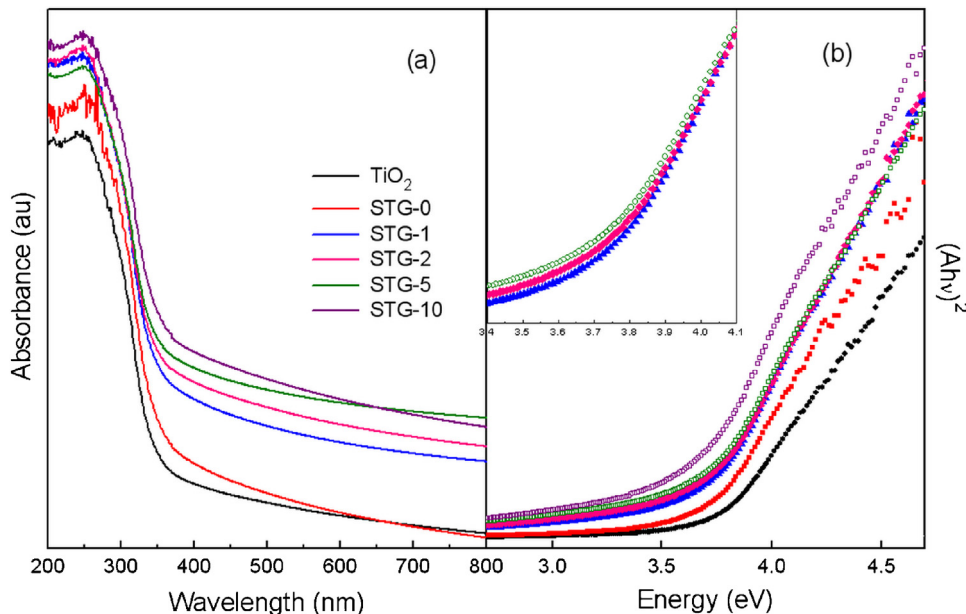


Fig. 7. UV-Vis-DRS spectra of the TiO_2 and STG-*i* samples.

Table 1

Textural properties and kinetic parameters of MO photocatalysis on nanosized TiO₂ and STG-*i* composites.

Sample	Nominal Sn content (mol%)	Atomic Sn/Ti ratio (%) ^a	Surface area (m ² g ⁻¹) ^b	Micropore area (m ² g ⁻¹) ^b	Pore volume (cm ³ g ⁻¹) ^b	Micropore volume (cm ³ g ⁻¹) ^b	Pore size (nm) ^b	k _{app} (min ⁻¹) ($\times 10^{-3}$) ^c	
								UV	Vis
P25	–	–	44	17.05	0.15	0.0098	16.03	6.64	0.65
TiO ₂	–	–	261	43.11	0.28	0.0211	3.87	1.16	–
STG-0	0	–	271	39.33	0.24	0.0185	3.21	3.66	1.09
STG-1	1	–	282	41.14	0.30	0.0147	3.92	2.63	2.91
STG-2	2	1.35	319	41.10	0.26	0.0154	3.04	8.64	3.71
STG-5	5	2.82	307	33.37	0.25	0.0119	3.06	7.15	4.53
STG-10	10	3.02	276	25.76	0.23	0.0095	3.12	8.57	3.96

^a Calculated from XPS analysis.

^b Determined by N₂ adsorption–desorption measurements.

^c Apparent first-order reaction rate constant, evaluated from the slope of the plot of ln(C/C₀) = -k_{app}t.

To evaluate the optical properties, UV–Vis–DRS spectra of the TiO₂ and STG composites were obtained; the results are shown in Fig. 7(a). The absorption edges of pristine TiO₂ and STG-0 were located at 380 and 385 nm, respectively. A red shift of the absorption edge toward longer wavelengths occurred upon the addition of RGO and increasing the amount of Sn dopant. This is ascribed to a reduction in the energy of excited photons, charge-transfer transitions, and therefore, band gap narrowing. The direct band gap energy was determined from the Tauc plot of (Ahv)² versus the photon energy [52] via the intercept of the tangent to the plot, as shown in Fig. 7(b). The band gap narrowed from 3.65 to 3.3 eV for STG-10, indicating charge transfer transitions between the three components. Moreover, tails around the higher wavelength region were observed on the spectra of the STG composite materials, implying possible use under visible light illumination. Hence, the incorporation of RGO and Sn species significantly changed the local electronic structure of TiO₂, and possibly its use in photocatalysis.

3.2. Photocatalytic activity measurement under UV and visible light irradiation

The role of Sn doping in the photocatalytic activity of the aforementioned composite materials was evaluated by measuring the rates of degradation of MO under both UV and visible light in the presence of the materials. Firstly, all the samples were conducted the adsorption in dark chamber until reached equilibrium after 2 h. The adsorption curves over P25, TiO₂ and STG composites were shown in Fig. S7 (see Supplementary material). It can be obviously seen that commercial P25 exhibited very low adsorption efficiency, <5%, compared to prepared nanosized TiO₂ (~40%) and STG materials. The adsorption significantly improved in the presence of RGO, remaining 40% of MO in the solution after 2 h. However, the adsorption behavior fluctuated with Sn doping content and it did not follow the trend in BET surface areas in Table 1. The results indicated that the addition of Sn was detrimental to adsorbability. Subsequently, Fig. 8(a) shows the normalized temporal concentration changes (C/C₀) of MO at given time intervals upon UV irradiation after dark adsorption. The presence of RGO significantly promoted the photodegradation of MO from 15% over nanosized TiO₂ up to 62% over STG-0. While the introduction of Sn at low concentrations inhibited the activity, a significant enhancement in the photodegradation conversion of MO to 87% after 210 min was observed when the Sn dopant concentration was increased. Generally, doping the STG composite materials with 2, 5, and 10 mol% Sn led to much higher photodegradation efficiencies than those observed for STG-0, STG-1, and pristine TiO₂. The decolorization performances of STG-2, STG-5, and STG-10 were comparable to that of commercial TiO₂ (P25, Degussa), a benchmark photocatalyst. Using the Langmuir–Hinshelwood first-order kinetic model [53,54], the apparent reaction rate constant, k_{app}, can be derived from plots of the linear logarithmic transform ln(C/C₀) = f(t) (shown

in Fig. 8(b)). As seen in Table 1, the STG-2 composite exhibited the highest k_{app} value, $8.64 \times 10^{-3} \text{ min}^{-1}$. This rate is about 2.4 times higher than that of STG-0. The order of the rates of catalytic activity of the composite materials toward degradation of MO is: STG-1 < STG-0 < STG-5 < STG-10 < STG-2. Much higher activities over STG-2, STG-5 and STG-10 can be attributed to the presence of Ti³⁺ and Sn²⁺ sites in the structure. It has been demonstrated that defect surface state, *i.e.* Ti³⁺, is a photocatalytic active site that plays the role of electron trapping center, effectively increase the separation of charge carriers [55]. Based on XPS result, increasing Sn doping resulted in higher Ti³⁺ and Sn²⁺ portion. However, there is always an optimal value and large quantity of such defect sites negatively affects the photocatalytic activity because that leads to the accumulation of photogenerated electrons in the conduction band. Due to the decrease in average distance between the trap sites, those electrons have tendency to reunite with holes, so they imperturbably become recombination centers that are unfavorable for the photocatalytic degradation. In this study, the results indicate that the incorporation of a high Sn concentration into the TiO₂/RGO system enhances the UV-photocatalytic degradation of organic or dye molecules. The photo-stability of STG-*i* photocatalysts was typically monitored through the cycle runs during three consecutive cycles of STG-2 composite, which showed the fastest rate constant. After each cycle, the MO-contaminated samples were collected from dye solution by centrifugation, washed thoroughly by deionized water several times, vacuum-dried overnight and then re-used. Fig. S8 (see Supplementary material) showed that the normalized efficiencies and rate constants did not change so much during several cycles, indicating the good durability of STG photocatalyst prepared in this study.

Fig. 9 displays the photodegradation ability of the STG composites under excitation with daylight. About 40–60% of the MO was photocatalytically degraded after 180 min exposure over the STG-*i* composite materials. Thus, it is apparent that the photocatalytic activity of the materials toward degradation of the organic molecule is enhanced with an increase of the Sn dopant amount from 1 to 5 mol%. In particular, STG-5 exhibited the best performance, leaving only 40% of the MO in the solution after 180 min, whereas TiO₂/RGO and P25 left 70% and 85% of the MO concentration, respectively, under the same conditions. The fastest rate constant over STG-5 was found to be $k_{\text{app}} = 4.53 \text{ min}^{-1}$, while a lower efficiency, 3.96 min^{-1} , was attained for STG-10. Thus, doping Sn into TiO₂ nanoparticles anchored onto RGO nanosheets accelerates the visible-light photoactivity, but excess doping concentrations do not facilitate improvements in the photoactivity. The good stability of STG-5 which is the best visible-light-driven photocatalyst for three consecutive cycles was also showed in Fig. S9 (Supplementary material).

Compared to the rate order obtained upon UV irradiation, it can be seen that the order under visible light is quite different, as follows: STG-0 < STG-1 < STG-10 < STG-5. The reproducibility tests

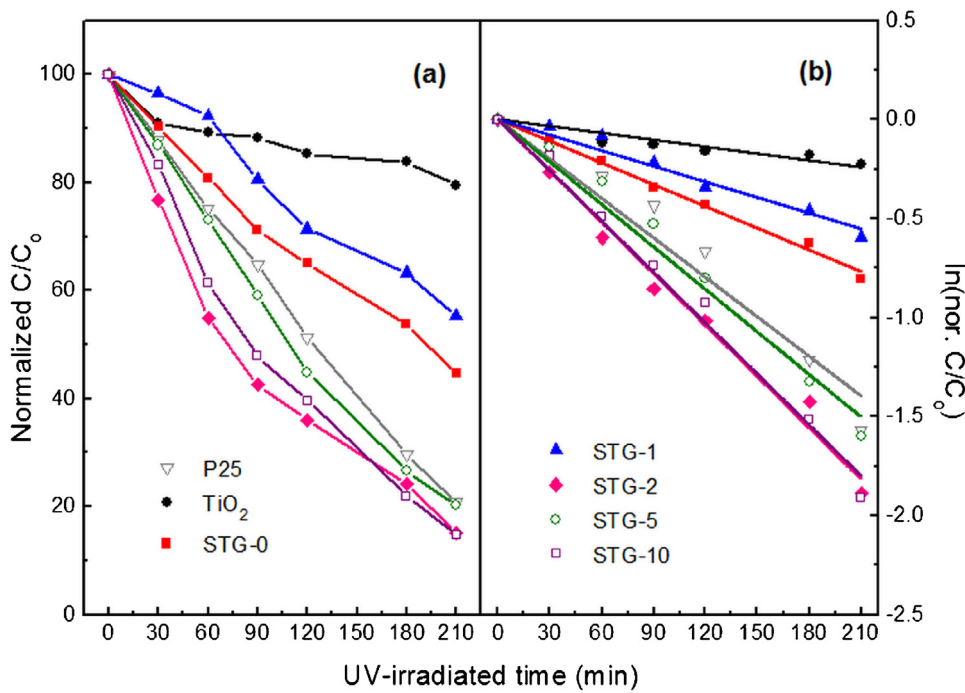


Fig. 8. (a) Photocatalytic degradation of methyl orange under UV irradiation and (b) apparent first-order kinetics over STG-*i* composites (when compared to commercial P25 and pristine TiO₂).

were conducted and negligible variation in the conversion and rate constant was attained, showing the virtually similar photocatalytic trend. The structural, chemical and electronic properties of the composites with their performances were connected to figure out such a different order, including the nature of Ti³⁺, Sn⁴⁺ and Sn²⁺ sites as well as the micro-mesoporous surface area. As mentioned above, the higher activities over the doped composites over 2 mol% Sn are stemming from higher portion of catalytic active sites, Ti³⁺ and Sn²⁺. Nevertheless, the fluctuation under UV light and the trend difference between two light exposure conditions cannot be

explained but they must be shown to demonstrate that these composites in the present study can work upon either UV or visible light.

Herein, the function of RGO in the composite materials was elucidated by comparing the adsorption and photocatalytic properties of pristine TiO₂ versus STG-0 as well as ST-2 (Sn-doped TiO₂ with 2 mol% Sn) versus STG-2 composite materials. As shown in Fig. S10 (see in Supplementary material), the adsorption ability of MO significantly increased from 45% over TiO₂ to 63% over STG-0 after 2 h. STG-2 sample removed 41% of the MO after 120 min, 10% higher than that over ST-2 material. Such findings can be

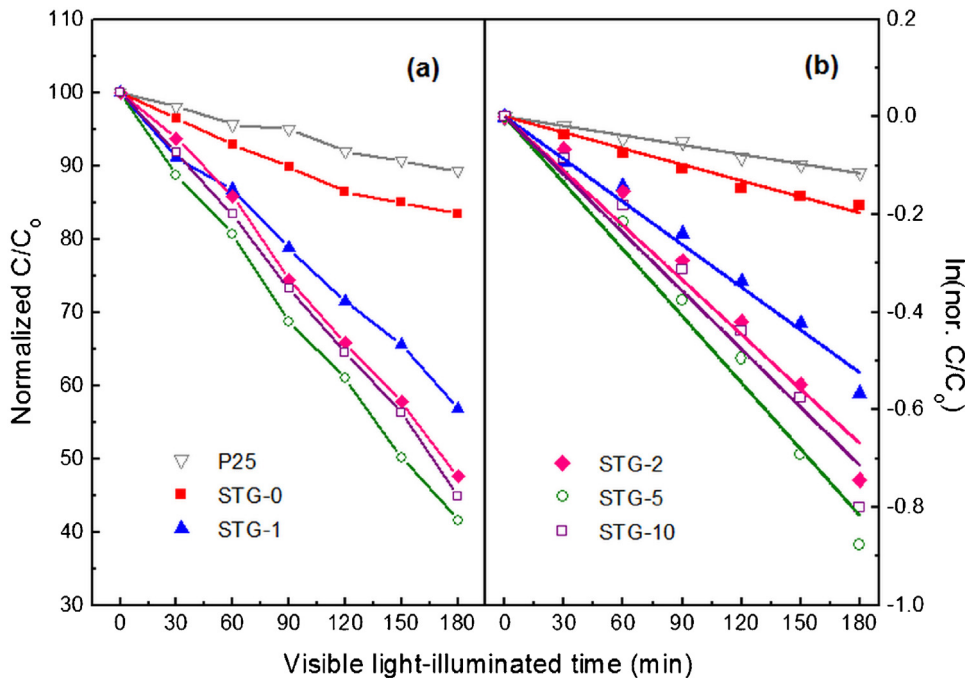
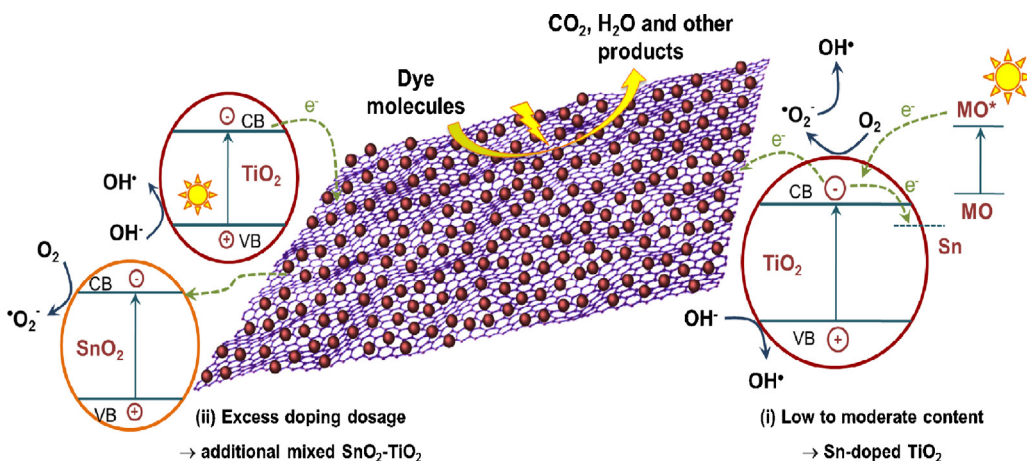


Fig. 9. (a) Visible-light photocatalytic performance and (b) degradation kinetics over the STG-*i* composites.



Scheme 1. Illustration of the electron transfer mechanism in the STG composites that significantly retards the geminate recombination of photo-induced electron–hole pairs, efficiently improving the photocatalytic performance under both UV and visible light illumination.

attributed to an enhancement in the surface area in the presence of RGO nanosheets, which enriched the accommodation and transportation of MO molecules on the surface, as shown in Table 1. In addition, with the introduction of two-dimensional RGO sheets containing abundant aromatic rings, the dye molecules can be easily adsorbed via π - π conjugation with offset face-to-face orientations, thereby increasing the adsorbability [20]. Furthermore, RGO sheets also affect the UV-photocatalytic activity, as shown in Fig. S11 (see in Supplementary material). The addition of RGO accelerated the mineralization of MO under UV exposure, which was 4-fold and 6-fold faster than that observed with pure TiO₂ and ST-2, respectively. Especially, the RGO has a strong influence on the activity obtained from visible light illumination (Fig. S12 in Supplementary material). Without RGO, ST-2 exhibited a low activity with a 4.5 times lower k_{app} value. It can be explained that the RGO sheets work as a photosensitizer that extends light absorption into the visible range, enabling the structures to work efficiently at any photoreponse condition [15,27]. Under visible light irradiation, electrons can be directly excited from the RGO to the conduction band of the metal oxides, thereby inducing hole doping in the RGO layer.

It is well-known that the specific surface area of a material is one of the key factors that affects its photocatalytic performance [26,56]. Nevertheless, in this study, the order of photoactivity did not follow the trends in the surface area of TiO₂/RGO composite materials after doping with Sn. Instead, the RGO sheets and Sn dopants induce modifications in the energy levels, particularly in the electron transfer direction. In the system of Sn-doped TiO₂ onto RGO, RGO first acts as an electron acceptor of excited electrons from the conduction band of TiO₂. Such charges are then transported to the π - π conjugational plane of RGO due to the higher work function of RGO ($\Phi_{GP} = -4.42$ eV versus vacuum) than that of TiO₂ ($\Phi_{TiO_2} = -4.2$ eV) [15,24,57]. Hudson [58] defined the “work function” as the minimum energy needed to move an electron from the Fermi level into vacuum. When different nanomaterials with different work functions are in contact, a Schottky barrier for electron transfer is formed at the nanojunction [59]. Electrons tend to transfer from a material with a lower work function to that with a higher one. Thus, the higher activity of STG-0 over pristine TiO₂ can be explained by this electron-transfer mechanism, whereby charge easily migrates from the conduction band of TiO₂ to RGO. This in turn decreases geminate recombination with valence-band holes. More photoelectrons are scavenged by surface adsorbed O₂, leading to the generation of reactive oxidative species (ROSs), i.e. OH· radicals [60]. In addition, more holes are able to migrate to the surface hydroxyl groups to produce OH. Secondly, as seen in Scheme 1, three mechanisms occurred simultaneously over the

STG-*i* composites. Apart from establishing an electron transfer pathway from the TiO₂ to RGO, the conduction band of Sn is at a lower energy level than that of TiO₂ because SnO₂ has a higher work function, $\Phi_{SnO_2} = -4.5$ eV [24,57]. Doping Sn species creates impurity energy level in band gap of TiO₂, also called mid-band level. Thus, excited electrons from TiO₂ are thermodynamically transferred to the conduction band of Sn or mid-band level. Otherwise, MO or surface adsorbed MO· radicals is also excited under light irradiation due to a self-photosensitized process, injecting electrons from the MO* to the TiO₂ or RGO. These electrons are subsequently transferred to the Sn level and continue to be trapped by dissolved oxygen so as to create as many ROSs as possible, which strongly degrade the MO molecules.

On the other hand, in case of mixed SnO₂/TiO₂ decorated onto RGO at excess doping amount (STG-10 sample), because of such difference in work function, the photoinduced electrons naturally transfer from conduction band of TiO₂ to RGO and subsequently to conduction band of SnO₂ via the mechanism of coupling second semiconductor (Scheme 1) [29]. Apart from the roles of adsorbent and photosensitizer, RGO sheets indeed work either as electron transporter or as electron mediator, constantly shuttling the electrons from TiO₂ to SnO₂. That remarkably facilitates the electron transport and efficiently suppresses the direct recombination, enhancing the photocatalytic activity.

Thus, in this report, the photocatalytic activity and efficiency of the TiO₂/GO composite materials toward degradation of MO under UV-visible light irradiation were greatly influenced by Sn doping. Sn doping strongly suppresses the recombination of photo-induced electron/hole pairs, thereby promoting the photodegradation efficiency of MO. Moreover, the synergistic effect of Sn doping and RGO incorporation narrows the band gap such that enhanced light harvesting is observed for the STG composite materials due to the extension of the photoreponse region of the material into the visible regime. This can be attributed to a downward shift of the bottom conduction band in TiO₂ for the case of Sn doping, leading to a reduction in the band gap and an extension of the photoreponse to longer wavelengths [61]. However, excess dopant concentrations can also be detrimental to the photocatalytic performance for two main reasons: (i) a large active surface area can be concealed by highly dispersed species, thereby preventing light penetration, and (ii) large quantity of defect sites (Ti³⁺, Sn²⁺) decreases the average distance between the trap sites and leads to the accumulation of photo-induced electrons in the conduction band, therefore, they tend to reunite with holes and imperturbably become recombination centers that are unfavorable for the photocatalytic degradation [29].

4. Conclusions

In this work, we reported a hydrothermal synthetic route for the preparation of composite materials composed of Sn-doped TiO₂ nanoparticles supported onto RGO. The synthesis resulted in Sn-doped TiO₂/RGO composite particles with a very small diameter of about 4–6 nm. When compared to the pristine materials, the incorporation of RGO and Sn dopants into TiO₂ significantly enhanced the specific surface area, narrowed the band gap energy, and red-shifted adsorption edge (toward the visible light region) in the materials. Increasing the amount of Sn dopant to optimal value facilitated photoactivity under both UV and visible light exposure. The incorporation of both RGO and Sn dopants significantly altered the electron transfer direction, inhibiting the possible recombination of photo-induced charge carriers and thus, improving the photocatalytic performance of the materials.

Acknowledgment

This research was supported by the Basic Science Research Program through the National Research Foundation of Korea (NRF) funded by the Ministry of Education, Science and Technology (no. 2010-0008810) and by the development program of a local park funded by the Ulsan Metropolitan City and MEST (Ministry of Education, Science and technology).

Appendix A. Supplementary data

Supplementary data associated with this article can be found, in the online version, at <http://dx.doi.org/10.1016/j.apcata.2013.12.030>.

References

- [1] K.S. Novoselov, A.K. Geim, S.V. Morozov, D. Jiang, Y. Zhang, S.V. Dubonos, I.V. Grigorieva, A.A. Firsov, *Science* 306 (2004) 666–669.
- [2] S. Stankovich, D.A. Dikin, G.H.B. Dommett, K.M. Kohlhaas, E.J. Zimney, E.A. Stach, R.D. Piner, S.T. Nguyen, R.S. Ruoff, *Nature* 442 (2006) 282–286.
- [3] Y. Si, E.T. Samulski, *Nano Lett.* 8 (2008) 1679–1682.
- [4] C.N.R. Rao, A.K. Sood, K.S. Subrahmanyam, A. Govindaraj, *Angew. Chem. Int. Ed.* 48 (2009) 7752–7777.
- [5] W. Poirier, F. Schopfer, *Nat. Nanotechnol.* 5 (2010) 171–172.
- [6] D.A.C. Brownson, D.K. Kampouris, C.E. Banks, *J. Power Sources* 196 (2011) 4873–4885.
- [7] N. Peimyoo, T. Yu, J. Shang, C. Cong, H. Yang, *Carbon* 50 (2012) 201–208.
- [8] Z. Liu, J.T. Robinson, X. Sun, H. Dai, *J. Am. Chem. Soc.* 130 (2008) 10876–10877.
- [9] A.V. Murugan, T. MuraliGanth, A. Manthiram, *Chem. Mater.* 21 (2009) 5004–5006.
- [10] J.L. Vickery, A.J. Patil, S. Mann, *Adv. Mater.* 21 (2009) 2180–2184.
- [11] K. Zhang, V. Dwivedi, C. Chi, J. Wu, J. Hazard. Mater. 182 (2010) 162–168.
- [12] X. Meng, D. Geng, J. Liu, M.N. Banis, Y. Zhang, R. Li, X. Sun, *J. Phys. Chem. C* 114 (2010) 18330–18337.
- [13] T. Xu, L. Zhang, H. Cheng, Y. Zhu, *Appl. Catal., B* 101 (2011) 382–387.
- [14] X. An, J.C. Yu, *RSC Adv.* 1 (2011) 1426–1434.
- [15] S. Morales-Torres, L.M. Pastrana-Martínez, J.L. Figueiredo, J.L. Faria, A.M.T. Silva, *Environ. Sci. Pollut. Res.* 19 (2012) 3676–3687.
- [16] S. Guo, G. Zhang, Y. Guo, J.C. Yu, *Carbon* 60 (2013) 437–444.
- [17] J.H. Byeon, Y.-W. Kim, *ACS Appl. Mater. Interfaces* 5 (2013) 3959–3966.
- [18] C. Chen, L. Wang, Y. Liu, Z. Chen, D. Pan, Z. Li, Z. Jiao, P. Hu, C.-H. Shek, C.M.L. Wu, J.K.L. Lai, M. Wu, *Langmuir* 29 (2013) 4111–4118.
- [19] W. Sun, T. Peng, Y. Liu, S. Xu, J. Yuan, S. Guo, X.-Z. Zhao, *J. Mater. Chem. A* 1 (2013) 2762–2768.
- [20] H. Zhang, X. Lv, Y. Li, Y. Wang, J. Li, *ACS Nano* 4 (2009) 380–386.
- [21] Y.H. Ng, I.V. Lightcap, K. Goodwin, M. Matsumura, P.V. Kamat, *J. Phys. Chem. Lett.* 1 (2010) 2222–2227.
- [22] T. Lu, Y. Zhang, H. Li, L. Pan, Y. Li, Z. Sun, *Electrochim. Acta* 55 (2010) 4170–4173.
- [23] B. Jiang, C. Tian, Q. Pan, Z. Jiang, J.-Q. Wang, W. Yan, H. Fu, *J. Phys. Chem. C* 115 (2011) 23718–23725.
- [24] J. Zhang, X. Xiong, X.S. Zhao, *J. Mater. Chem.* 21 (2011) 3634–3640.
- [25] L.-Y. Chen, W.-D. Zhang, B. Xu, Y.-X. Yu, *J. Nanosci. Nanotechnol.* 12 (2012) 6921–6929.
- [26] R. Leary, A. Westwood, *Carbon* 49 (2011) 741–772.
- [27] A. Du, Y.H. Ng, N.J. Bell, Z. Zhu, R. Amal, S.C. Smith, *J. Phys. Chem. Lett.* 2 (2011) 894–899.
- [28] G. Liu, L. Wang, H.G. Yang, H.-M. Cheng, G.Q. (Max) Lu, *J. Mater. Chem.* 20 (2010) 831–843.
- [29] S.G. Kumar, L.G. Devi, *J. Phys. Chem. A* 115 (2011) 13211–13241.
- [30] F. Fresno, C. Guillard, J.M. Coronado, J.-M. Chovelon, D. Tudela, J. Soria, J.-M. Herrmann, *J. Photochem. Photobiol. A* 173 (2005) 13–20.
- [31] J. Liqiang, F. Honggang, W. Baiqi, W. Dejun, X. Baifu, L. Shudan, S. Jiazhong, *Appl. Catal., B* 62 (2006) 282–291.
- [32] J. Li, H.C. Zeng, *J. Am. Chem. Soc.* 129 (2007) 15839–15847.
- [33] C. Xiong, K.J. Balkus Jr., *J. Phys. Chem. C* 111 (2007) 10359–10367.
- [34] Y. Cao, T. He, L. Zhao, E. Wang, W. Yang, Y. Cao, *J. Phys. Chem. C* 113 (2009) 18121–18124.
- [35] M. Xu, P. Da, H. Wu, D. Zhao, G. Zheng, *Nano Lett.* 12 (2012) 1503–1508.
- [36] N. Farhangi, R.R. Chowdhury, Y. Medina-Gonzalez, M.B. Ray, P.A. Charpentier, *Appl. Catal., B* 110 (2011) 25–32.
- [37] Y. Hou, F. Zuo, A. Dagg, P. Feng, *Nano Lett.* 12 (2012) 6464–6473.
- [38] Y. Shi, S.-L. Chou, J.-Z. Wang, D. Wexler, H.-J. Li, H.-K. Liu, Y. Wu, *J. Mater. Chem.* 22 (2012) 16465–16470.
- [39] W. Fan, W. Gao, C. Zhang, W.W. Tjiu, J. Pan, T. Liu, *J. Mater. Chem.* 22 (2012) 25105–25115.
- [40] Y. Luo, J. Luo, W. Zhou, X. Qi, H. Zhang, D.Y.W. Yu, C.M. Li, H.J. Fan, T. Yu, *J. Mater. Chem. A* 1 (2013) 273–281.
- [41] L. Jiang, R. Zou, W. Li, J. Sun, X. Hu, Y. Xue, G. He, G. Hu, *J. Mater. Chem. A* 1 (2013) 478–481.
- [42] P. Roy, A.P. Periasamy, C.-T. Liang, H.-T. Chang, *Environ. Sci. Technol.* 47 (2013) 6688–6695.
- [43] W.S. Hummers, R.E. Offeman, *J. Am. Chem. Soc.* 80 (1958) 1339.
- [44] P. Patnaik, *Handbook of Inorganic Chemicals*, McGraw Hill, New York, NY, 2003.
- [45] Z.L. Liu, Z.L. Cui, Z.K. Zhang, *Mater. Charact.* 54 (2005) 123–129.
- [46] V. Štengl, S. Bakardjieva, N. Murafa, *Mater. Chem. Phys.* 114 (2009) 217–226.
- [47] F. Tuinstra, J.L. Koenig, *J. Chem. Phys.* 53 (1970) 1126–1130.
- [48] S. Kelly, F.H. Pollak, M. Tomkiewicz, *J. Phys. Chem. B* 101 (1997) 2730–2734.
- [49] C.D. Wagner, W.M. Riggs, L.E. Davis, J.F. Moulder, *Handbook of X-ray Photoelectron Spectroscopy*, Perkin-Elmer Corp., Physical Electronics Division, Eden Prairie, MN, 1978.
- [50] M.G. Mason, *Phys. Rev. B: Condens. Matter* 27 (1983) 748–762.
- [51] T.L. Barr, *J. Vac. Sci. Technol., A* 9 (1991) 1793–1805.
- [52] J. Tauc, *Amorphous and Liquid Semiconductors*, Plenum, London, 1974.
- [53] J. Matos, J. Laine, J.-M. Herrmann, *Appl. Catal., B* 18 (1998) 281–291.
- [54] A. Houas, H. Lachheb, M. Ksibi, E. Elaloui, C. Guillard, J.-M. Herrmann, *Appl. Catal., B* 31 (2001) 145–157.
- [55] V. Štengl, D. Popelková, P. Vláčil, *J. Phys. Chem. C* 115 (2011) 25209–25218.
- [56] A. Kudo, Y. Miseki, *Chem. Soc. Rev.* 38 (2009) 253–278.
- [57] M. Grätzel, *Nature* 414 (2001) 338–344.
- [58] J.B. Hudson, *Surface Science: An Introduction*, John Wiley and Sons, New York, NY, 1998.
- [59] R. Dalven, *Introduction to Applied Solid State Physics*, second ed., Plenum Press, New York, London, 1990.
- [60] Z. Xiong, L.L. Zhang, J. Ma, X.S. Zhao, *Chem. Commun.* 46 (2010) 6099–6101.
- [61] R. Long, Y. Dai, G. Meng, B. Huang, *Phys. Chem. Chem. Phys.* 11 (2009) 8165–8172.